mater.scichina.com link.springer.com

Sci China Mater 2025, 68(8): 2775–2782
https://doi.org/10.1007/s40843-025-3452-9

Mixed ionic/electronic conducting framework enabled by transition metal-ion reduction in Li-LLTO composite anodes for ultrafast lithium diffusion

Huilin Zhu[1], Shiwei Deng[1], Xinyi Kong[1], Xing Xiang[2], Yan Duan[1], Jian-Fang Wu[1*] and Jilei Liu[1*]

ABSTRACT **The development of $Li_7La_3Zr_2O_{12}$ (LLZO) solid electrolytes is challenged by the unstable Li/LLZO interface during lithium stripping and plating processes, which impedes interfacial charge transport and accelerates lithium dendrite growth. Here, a freestanding ultrathin Li-$Li_{0.3}La_{0.5}TiO_3$ (LLTO) composite anode with a three-dimensional interconnected mixed ionic/electronic conducting LLTO framework was developed. The mixed ionic/electronic conduction of LLTO arises from the *in-situ* reduction of transition metal ions (Ti^{4+}) by metallic lithium. The Li-LLTO composite anode possesses good affinity toward LLZO solid electrolytes, achieving a low interfacial resistance of 11.7 Ω cm^2, and a high lithium self-diffusion coefficient reaching 4.5×10^{-11} cm^2/s, about one order of magnitude higher than that of pure lithium anode. These features collectively enhance the Li-LLTO/LLZO interfacial stability, increasing the critical current density fourfold and enabling a 1300-h symmetrical cell cycling life. It delivers high-performance solid-state lithium batteries with an 80% capacity retention after 220 cycles. This advancement not only improves the performance of lithium metal anodes in solid-state batteries but also offers promising insights for next-generation high-energy-density electrochemical energy storage systems.**

Keywords: garnet electrolyte, lithium-metal anodes, mixed ionic/electronic conduction, diffusion kinetics, interface stability

INTRODUCTION

The tremendous interest in the safe and high-density electrochemical energy storage system has brought all-solid-state lithium batteries (ASSLBs) to the forefront of battery research, driven by the good compatibilities with high-voltage cathodes and metallic lithium anode of solid electrolytes (SEs) [1–7]. Among various SEs, cubic doped $Li_7La_3Zr_2O_{12}$ (LLZO) garnets, for example $Li_{6.4}La_3Zr_{1.4}Ta_{0.6}O_{12}$, deliver a high lithium-ion conductivity (>1 mS/cm at room temperature), wide electrochemical window (> 5 V vs. Li^+/Li), and electrochemical stability with metallic lithium anode [8–13]. As a result, LLZO-based ASSLBs have demonstrated attractive electrochemical performances and become a major research focus in the field of the ASSLBs. However, the poor interfacial stability, including the volatile lithium stripping and plating and uncontrollable lithium dendrites, severely degrades the electrochemical performances of the LLZO-based ASSLBs [14–16]. Key factors contributing to these issues have been uncovered, including the electronic conductivity of LLZO SEs [17], poor contact at the electrode/LLZO interface [18] and low self-diffusion coefficient of lithium in the pure lithium anode [19–21]. Consequently, interfacial modification to enhance the affinity of SEs to electrode [22–25], composite LLZO SEs with decreased electronic conductivity [26,27] and design of metallic lithium anodes [28–31] have been implemented to ameliorate the poor interfacial stability. Furthermore, the electrochemical performance of the battery can be further improved through the rational design of electrode and SE materials [32–36]. Great achievements have been attained with the stable lithium stripping and plating current density reaching several milliamperes per square centimeter, approaching that in metallic lithium batteries with liquid electrolytes.

Notably, the critical current density of stable lithium stripping and plating was enhanced to 100 mA/cm^2 at room temperature by penetrating metallic lithium into three-dimensional (3D) porous LLZO layers [37]. It can be considered as a composite lithium anode with LLZO embodied in the metallic lithium matrix. A collaborative migration of lithium and electrons can occur on the Li/LLZO interface in the composite, resulting in optimized lithium diffusion kinetics. This phenomenon has also been reported and confirmed on the interface of $RbAg_4I_5$/graphite composite [38]. Another lithium-ion conductor, perovskite $Li_{0.3}La_{0.5}TiO_3$ (LLTO), was blended with the metallic lithium to improve the stability of the lithium stripping and plating and to suppress the lithium dendrites on the Li/LLZO interface [39]. However, the chemical reaction between the LLTO and metallic lithium which determines the lithium diffusion along the Li/LLTO interface is still unclear.

In this study, we fabricated 20 μm freestanding Li-LLTO composite anodes, with 3D interconnected mixed ionic/electronic conductive framework, by incorporating LLTO particles into the metallic lithium using an *in-situ* reduction method. Compared with pure lithium anodes, the self-diffusion coefficient of lithium in Li-LLTO composite anodes is approximately one order of magnitude higher, which also enhanced the Li-LLTO/AlF_3-LLZTO interface contact and effectively inhibited the growth of lithium dendrites (Fig. 1a). The mixed ionic/electronic conductive framework was constructed by the *in-situ* reduction of transition metal ions in LLTO (namely Ti^{4+} ions), along which electrons generate (Fig. 1b). To firmly demonstrate the reactions between metallic lithium and LLTO in the com-

[1] College of Materials Science and Engineering, Hunan Joint International Laboratory of Advanced Materials and Technology of Clean Energy, Hunan University, Changsha 410082, China
[2] Hubei Provincial Key Laboratory of Green Materials for Light Industry, Hubei University of Technology, Wuhan 430068, China
* Corresponding author (email: jfwu@hnu.edu.cn; liujilei@hnu.edu.cn)

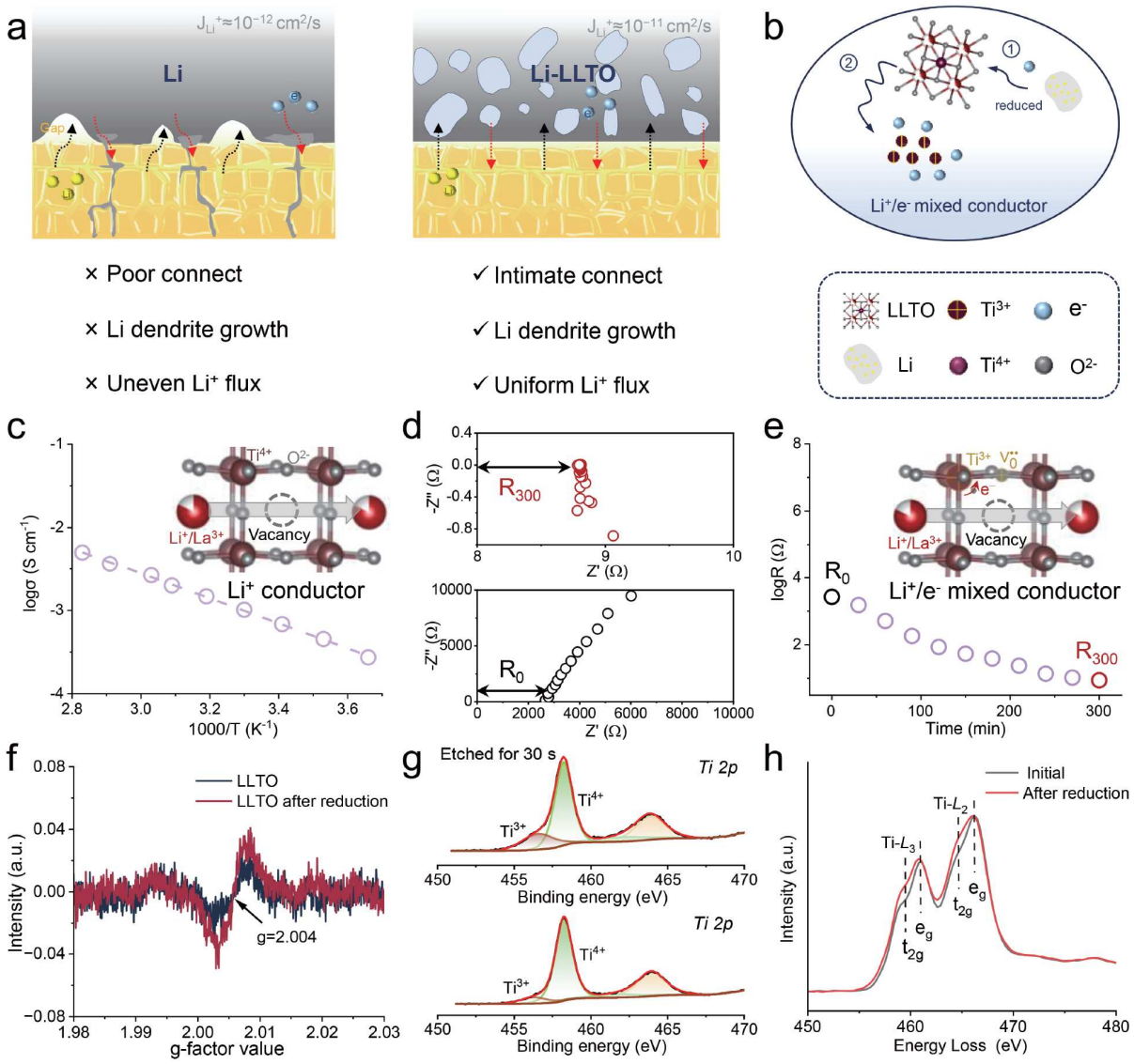

Figure 1 (a) Schematic illustration of interfacial stability using the pure lithium and Li-LLTO composite anode. (b) Possible reactions between LLTO and Li. (c) Bulk conductivities of LLTO at different temperatures. The inset shows lithium-ion migration pathways within LLTO. (d) Impedance spectra of the Li/LLTO/Li symmetric cell in initial state (down) and after 300 min (upper). (e) Temporal evolution of resistance of the Li/LLTO/Li symmetric cell calculated from the impedance spectra, and the schematic diagram of the mixed ionic/electronic conduction produced in the process. (f) EPR spectra of LLTO before and after the reaction with lithium. (g) XPS diagram of Ti 2p of LLTO before (down) and after (upper) reaction with lithium. (h) Ti-$L_{2,3}$ EELS data of LLTO before and after the reaction.

posite lithium anode and their consequences, the composition and structure of the Li-LLTO composite anode were systematically studied. The application of Li-LLTO composite anodes in AlF_3-LLZTO-based solid-state batteries was also evaluated using symmetrical cells and full cells.

RESULTS AND DISCUSSION

Transition metal-ion reduction of LLTO by metallic lithium

The LLTO possesses a tetragonal perovskite structure (Fig. S1), where Li^+ ions, La^{3+} ions and vacancies share the same site, and Li^+ ions migrate among the lattice sites and vacancies (Fig. 1c). The grain bulk resistance and grain-boundary resistance of dense LLTO ceramics (Fig. S2) are respectively 287 and 11151 Ω, fitted from the typical impedance spectrum as shown in Fig. S3. The grain bulk conductivity was calculated to be 0.68 mS/cm at 20 °C. The lithium-ion conductivity is related to the temperature according to the Arrhenius equation (Fig. 1c), with an activation energy of 0.3 eV. The lithium-ion conductivity and the activation energy are in concert with results in literatures [40,41].

To study the introduction of electronic conduction into LLTO, a symmetrical cell as shown in Fig. S4 was constructed by pressing two pieces of lithium anodes on the LLTO ceramic. The resistance of the cell was monitored in 300 min (Fig. S5). Initially, the cell delivered a huge resistance of about 80000 Ω, with a high-frequency intercept resistance of ~2500 Ω (Fig. 1d, R_0). This initial resistance was larger than the grain bulk resistance of LLTO and was attributed to the insufficient contact between the LLTO and lithium anodes. Over time, the battery resistance and the intercept resistance decreased, eventually resulting in a

resistance of ~9 Ω without the semi-circle (Fig. 1d). The decrease in intercept resistance over time is illustrated in Fig. 1e, with an extremely low resistance (R_{300}) caused by the electronic conduction in the LLTO. Considering the strong reduction of metallic lithium, the electronic conduction in LLTO originates from two possible mechanisms following the equations.

$$Li+Ti_{Ti}^{\times} \rightarrow Ti_{Ti}^{\prime}+Li^{+}. \quad (1)$$

The Ti^{4+} in its lattice site ($Ti_{Ti}^{\times}$) can be reduced to Ti^{3+}, or other lower valence states. Additionally, the metallic lithium can capture oxygen, creating oxygen vacancies in LLTO following Equation (2).

$$2Li+O_{O}^{\times} \rightarrow V_{O}^{\cdot\cdot}+2e'+Li_2O. \quad (2)$$

Free electrons can be generated through the activation of excess electrons around Ti nuclei, as well as during the formation of oxygen vacancies.

The electron paramagnetic resonance (EPR) results are exhibited in Fig. 1f, and the EPR is an effective method to detect the oxygen vacancies in LLTO by examining unpaired electrons in materials. Both the initial LLTO and the LLTO after reduction uniquely exhibit a symmetrical ESR signal at g = 2.004, manifesting the electron trapping at oxygen vacancies [42]. Although the signal strength of the reduced LLTO is higher, the difference is insignificant, indicating that the formation of oxygen vacancies may not be the key factor for LLTO's electronic conduction. X-ray photoelectron spectroscopy (XPS) results of Ti, O, La and Li elements in the samples before and after reduction are also shown in Fig. 1g and Fig. S6. The peaks located at 458.2 and 456.6 eV can be attributed to the Ti^{4+} and Ti^{3+} in the Ti 2p XPS plots. It is clear that the peak intensity of Ti^{3+} in the reduced sample is obviously larger than that of the initial LLTO. The relative contents of Ti^{3+} to Ti^{4+} in the two samples were estimated by the peak area ratio, which is 0.34 of the reduced sample, while that of the initial sample is 0.07. Notably, the content of oxygen vacancies in the reduced sample (0.28) is slightly higher than that of the initial sample (0.22), as concluded from the relative peak area of oxygen vacancies to that of the lattice oxygen (Fig. S7). Additionally, the Li 1s and La $3d_{5/2}$ spectra (Fig. S6) confirm unchanged valence states. To further verify the electron generation in LLTO, the valence states of elements before and after the reduction of LLTO were investigated using high-resolution transmission electron microscopy (TEM) coupling electron energy loss spectroscopy (EELS). Fig. 1h shows the Ti-$L_{2,3}$ edge of LLTO before and after the reduction. The changes in the Ti-$L_{2,3}$ edge are caused by electron transitions from the inner Ti 2p orbitals to the unoccupied Ti 3d orbitals [43,44]. In the reduced sample, the Ti-$L_{2,3}$ edge shifts to lower energies, and the pre-peak intensities of the Ti-L_3 and Ti-L_2 edges are significantly lower than those in the initial sample. These phenomena indicate an increase in the number of d electrons in Ti and the reduction of Ti^{4+} to Ti^{3+}. In addition, the pre-peak intensity of the O-K edge is associated with the hybridization between O 2p and Ti 3d orbitals [43]. The pre-peak intensity of the O-K edge of the reduced sample in Fig. S8c is significantly lower than that of the initial sample, indicating a decrease in the oxygen content within the coordination shell of Ti, which implies the formation of oxygen vacancies. In contrast, no significant difference was observed in the EELS spectra of La (Fig. S8b), which was due to the absence of valence change of La, consistent with the above XPS results. Therefore, the electronic conduction in LLTO is mainly caused by the reduction reaction between Ti^{4+} and the metallic lithium according to Equation (1), with the oxygen vacancies formation in Equation (2) also playing a contributing role. The LLTO after the reaction remains a similar crystalline phase to the initial sample (Fig. S9). Thus, mixed ionic/electronic conduction was produced by the main transition metal reduction of Ti and the secondary formation of oxygen vacancies.

Analysis of Li-LLTO composite anodes

The Li-LLTO composite anodes were prepared by an *in-situ* reduction and rolling technique, and the composition and structure were systematically studied as shown in Fig. 2 and Figs S10–S13. The XRD patterns clearly show that the Li-LLTO composite anodes consist of cubic phase LLTO and metallic lithium (Fig. S10), along with broad peaks attributed to the Kapton tape. Furthermore, with increasing LLTO content in the composite anodes, the relative strength of the peak at ~30° (LLTO) to that of the peak at ~35° (Li) increases sharply. The relative content of LLTO in the composite anode will remarkably influence the property of the composite anode. We successfully prepared ultrathin composite lithium anodes with a thickness of ~22 μm (Fig. 2a). The ultrathin anodes are expected to diminish excess lithium in the battery and thus increase the energy density. The surface of the composite anode is relatively smooth with some relucent particles, which may be the LLTO of high molar weight (Figs S11 and S12). The particle size of the LLTO is non-uniform but the interface contact between the metallic lithium and the LLTO is quite intimate, which is beneficial to the diffusion of lithium through the interface. As shown in Fig. 2b and Fig. S13, the LLTO particles are homogeneously distributed in the composite anode, and the LLTO forms an interconnected framework in the composite. Based on the ionic/electronic conduction of the LLTO after contacting and *in-situ* reacting with the metallic lithium, mixed ionic/electronic conducting framework corbelled ultrathin freestanding composite lithium anodes were successfully obtained.

Interfacial compatibility of Li-LLTO composite anodes to garnet SEs

To assess the compatibility of this composite anode with garnet SEs, the AlF_3-LLZTO SEs with reduced electronic conductivity were prepared according to our previous work [45]. The interfacial affinity, interfacial resistance and cycling stability against lithium dendrites were then studied. As shown in Fig. S14, the interfacial contact angle between the SE and the Li-LLTO composite anode at 300 °C is almost 0°. The interfacial microstructure (Fig. 2c) clearly shows a conformal interface without any visible pores or delamination. Symmetrical cells using SEs and Li-LLTO composite anodes with different LLTO contents were assembled, and the interfacial resistances were respectively calculated to be 13.4, 13.5 and 11.7 Ω cm^2 for the Li-LLTO composite anodes with 40, 60 and 80 wt% LLTO (Fig. 2d) using electrochemical impedance spectroscopy (EIS, Fig. S15). Compared with the Li/AlF_3-LLZTO interface [45], the composite anode further attenuates the interfacial resistance and reinforces the interfacial ionic transport. Furthermore, the interfacial resistances are also comparable to those obtained through interfacial modifications [46–50].

Using the relationship between $-Z''$ and $\omega^{-1/2}$ for the Li-LLTO composite anodes with 40, 60 and 80 wt% LLTO (Fig. 2e), the

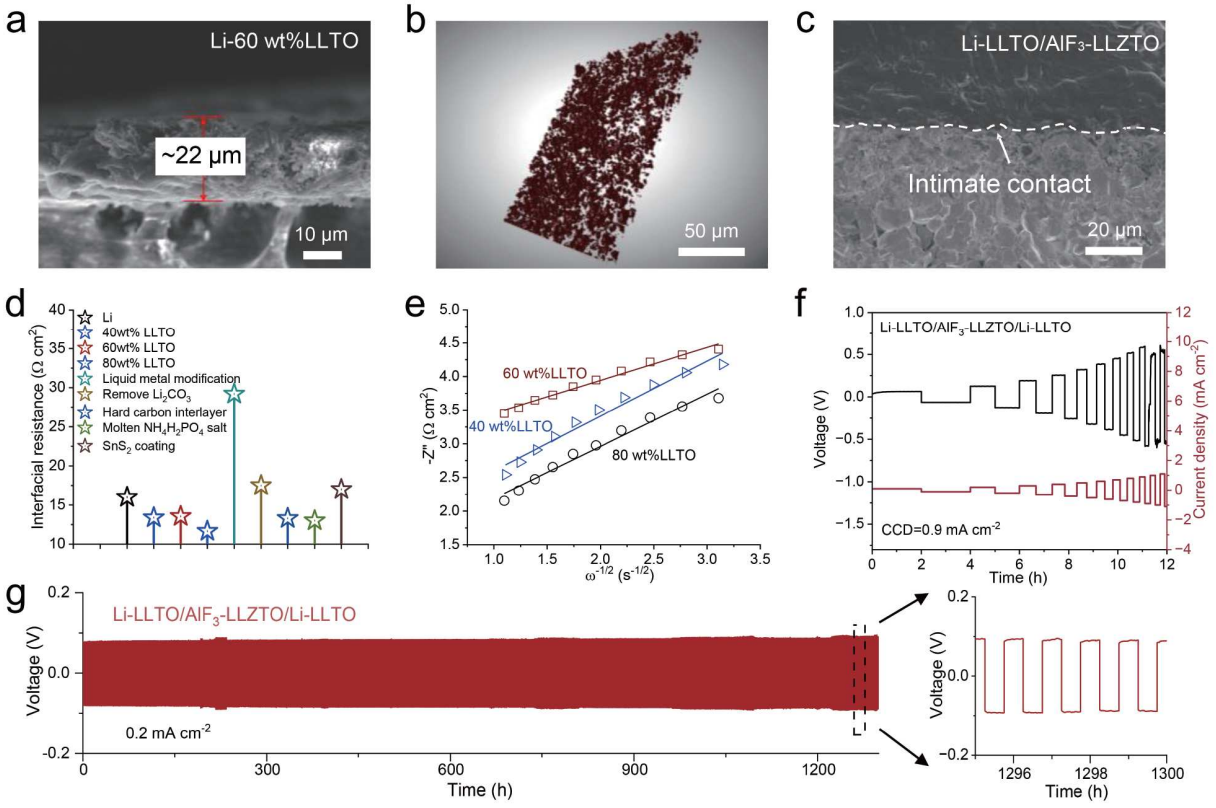

Figure 2 (a) Cross-sectional SEM image of the Li-60 wt% LLTO composite anode. (b) XCT (X-ray computed tomography) image of the Li-LLTO composite anode. (c) SEM image of the Li-LLTO/AlF_3-LLZTO interface. (d) Interfacial impedance of Li-LLTO composite anodes with different LLTO contents, and some recent results in the literatures are also shown as a comparison [45–50]. (e) Warburg coefficients of Li-LLTO/AlF_3-LLZTO/Li-LLTO symmetric cells using Li-LLTO composite anodes. (f) Critical current density and (g) galvanostatic cycling performances of Li-LLTO/AlF_3-LLZTO/Li-LLTO cell using Li-LLTO composite anodes with 60 wt% LLTO at 25 °C.

self-diffusion coefficients of lithium were estimated to be 1.5×10^{-11}, 4.5×10^{-11} and 1.8×10^{-11} cm^2/s, respectively. The self-diffusion coefficient of lithium in the Li-LLTO composite anode with 60 wt% LLTO was improved by one order of magnitude compared with the value of pure metallic lithium [51], which should be contributed to the 3D interconnected LLTO framework of mixed ionic/electronic conduction. In this composite, the interface between Li and LLTO acts as a fast transport pathway of lithium, which has been convincingly demonstrated in other composite electrodes [38,52,53]. The optimized self-diffusion coefficient benefits to the interfacial stability of the lithium stripping and plating [19,21,54]. The critical current densities for the symmetrical cells using Li-LLTO composite anodes with 40, 60 and 80 wt% LLTO are respectively 0.4, 0.9 and 0.5 mA/cm^2 (Fig. 2f and Fig. S16). These values are higher than the critical current density of the Li/AlF_3-LLZTO/Li cell (0.2 mA/cm^2) [45]. The critical current density of stable lithium stripping and plating is related to the self-diffusion coefficient of lithium in the metallic anode and the interfacial affinity, which were ameliorated by incorporating mixed ionic/electronic conducting LLTO with modulating its relative content. Moreover, the long-term stability of the symmetric cell was also studied under a fixed current density of 0.2 mA/cm^2 at room temperature (Fig. 2g). The cell reveals a stable polarization voltage 0.08–0.1 V in about 1300 cycles which can be attributed to the stable interface under cycling. The long-term cycling performance of the Li-LLTO composite anode with 60 wt% of LLTO coupled with AlF_3-LLZTO and Al_2O_3-LLZTO was also evaluated, as shown in Fig. S17. These symmetrical cells also do not show any sudden drop of polarization voltages, which are also better than the cell using pure lithium [45].

Interfacial lithium stripping and plating analysis

The interfacial microstructure after the lithium stripping and plating was examined using scanning electron microscopy (SEM) and is shown in Fig. 3 and Fig. S18. Under a current density of 0.2 mA/cm^2, the Li-LLTO/AlF_3-LLZTO interface delaminated after the stripping process (Fig. 3a). Meanwhile, the lithium plated along the interface homogeneously without forming any pores or cracks (Fig. 3b and Fig. S18). Tailoring the applied current density to a low value of 0.05 mA/cm^2, similar phenomena were observed at the interface during stripping and plating (Fig. 3c, d). Owing to the delamination of the Li-LLTO composite anode in the stripping process, the residual anode after stripping was peeled easily from the SEs by a scalpel, and the surface morphology was tested by SEM. There are discernible exposed LLTO particles, where the metallic lithium around them were stripped out, and the resultant pores are shown in Fig. 3e. Therefore, the bulk lithium atoms in the Li-LLTO composite anode are accessible during the stripping process due to the high self-diffusion coefficient, contributing to the improved cycling stability [55].

The internal resistance of the symmetrical cell was *in-situ* detected using EIS in the stripping and plating processes under a

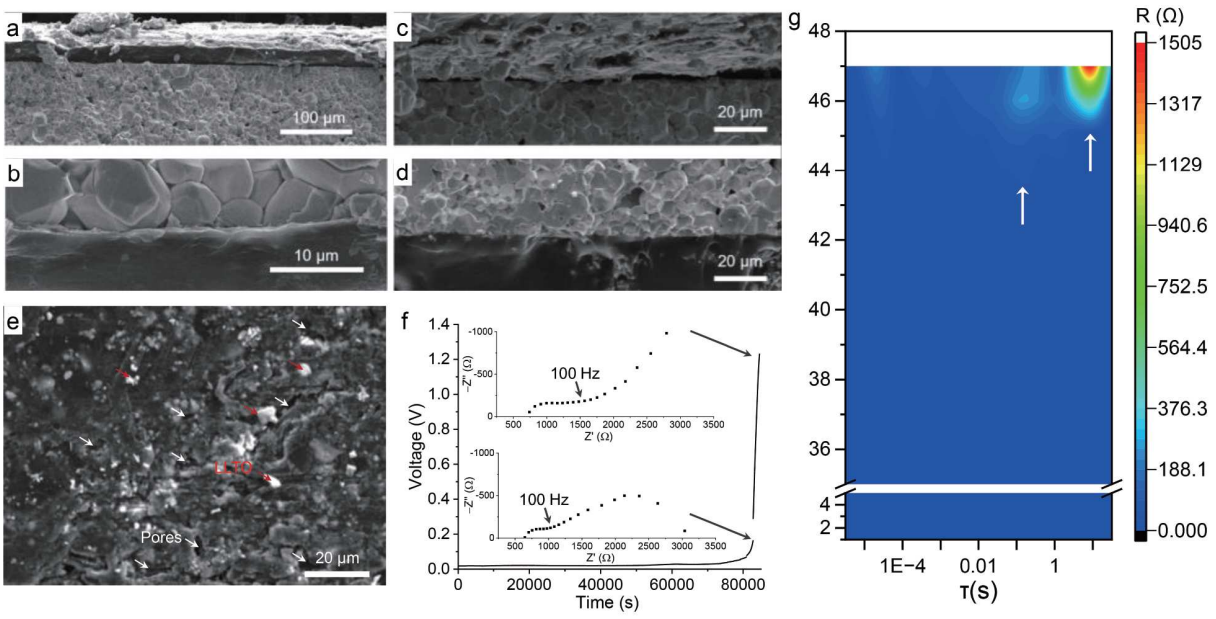

Figure 3 SEM images of the interface between the AlF_3-LLZTO and the Li-LLTO after the stripping (a, c) and plating (b, d) process under current densities of (a, b) 0.2 and (c, d) 0.05 mA/cm^2. (e) SEM image of the surface morphology of Li-LLTO composite anodes peeled from the symmetrical cell on the stripping side. (f) Evolution of the polarization voltage of the symmetrical cell in the stripping and plating process. The insets are the corresponding impedance spectra at 46th and 47th steps. (g) Evolution diagram of relaxation time distribution with test steps.

current density of 0.05 mA/cm^2 (Fig. 3f and Fig. S19). The EIS spectrum was obtained every 30 min until the polarization voltage reaches 1.2 V as shown in Fig. 3f. On the interface with lithium stripping, there are pores and delamination which induce high interfacial resistance. The internal resistance increases to ~3000 Ω after stripping for 83000 s (inset in Fig. 3f, down). However, lithium-ion transport still occurs at the interface during lithium stripping, as evidenced by the finite interfacial resistance value. After another 30-min stripping, an obvious oblique line appears in the low frequency zone of the impedance spectrum (inset in Fig. 3f, upper), indicating the interface has become lithium-ion blocking. In this case, the interface totally delaminated due to all the accessible lithium atoms stripping out at the given current density. The EIS spectra were translated into plots of distribution of relaxation time (τ, Fig. S20) and its evolution with the testing steps was exhibited in Fig. 3g. In 47 steps, the resistance change is negligible within the relaxation time below 0.01 s, which originates from the resistances of the SE and the interface with lithium plating. As a comparison, the resistance increases observably from the 43th step within the relaxation time from 0.01 to 1 s. The resistance increases sharply from the 45th step within the relaxation time from 1 to 32 s. The sharp increases of resistance within the relaxation time from 0.01 to 32 s are caused by the interfacial delamination.

Electrochemical performances of solid-state lithium batteries

$LiCoO_2$/AlF_3-LLZTO /Li-LLTO batteries were assembled as shown in Fig. 4a. Their electrochemical performances were studied at 45 °C in a voltage range of 2.5–4.2 V. The charge-discharge curves in Fig. 4b show the voltage platform of the battery at different rates. The battery delivers initial charge and discharge capacities of 155 and 129 mAh/g under the rate of 0.1 C (Fig. 4c), respectively. The initial Coulombic efficiency is about 83%. In five cycles under the rate of 0.1 C, the discharge capacity remains ~130 mAh/g, and the charge capacities are decreased to ~140 mAh/g. When the rates reach 0.2, 0.5, 1 and 2 C, the discharge capacities are ~132, ~128, ~120 and ~110 mAh/g, respectively. The capacities of the battery decrease with the increasing charge and discharge rate, but when the rate gets back to the lower values, the charge and discharge capacities recover. Additionally, the long-term cycling performance of the battery was also tested with a rate of 0.2 C (Fig. 4d, e). The initial charge and discharge capacities are 168.5 and 139.6 mAh/g, respectively. After 220 cycles, these values decrease to 113 and 112 mAh/g, respectively, and the corresponding retention ratio of discharge capacity is 80%. The battery using the Li-LLTO composite anodes possesses superior rate and long cycling performances comparable with other solid-state batteries using the garnet SEs [56–59] or $LiCoO_2$ cathodes [60,61].

CONCLUSIONS

Herein, freestanding ultrathin Li-LLTO composite anodes with 3D interconnected mixed ionic/electronic conducting LLTO framework was constructed. Using a combination of EIS, XPS, EPR, TEM and EELS, the ambiguous chemical reaction between LLTO and metallic lithium, governing lithium diffusion at the Li/LLTO interface, was elucidated. The composite anode possesses good affinity toward the AlF_3-LLZTO SEs inducing a low interfacial resistance of 11.7 Ω cm^2, and a high self-diffusion coefficient of lithium reaching 4.5×10^{-11} cm^2/s, about one order of magnitude higher than that of pure metallic lithium. These features enhance the Li-LLTO/AlF_3-LLZTO interfacial stability, increasing the critical current density fourfold and enabling a long cycling life for the symmetrical cells. Furthermore, the composite anode delivers high-performance solid-state lithium batteries with 80% capacity retention after 220 cycles. This advancement not only improves the performance of lithium metal anodes in solid-state batteries but also offers promising insights for next-generation high-energy-density electrochemical

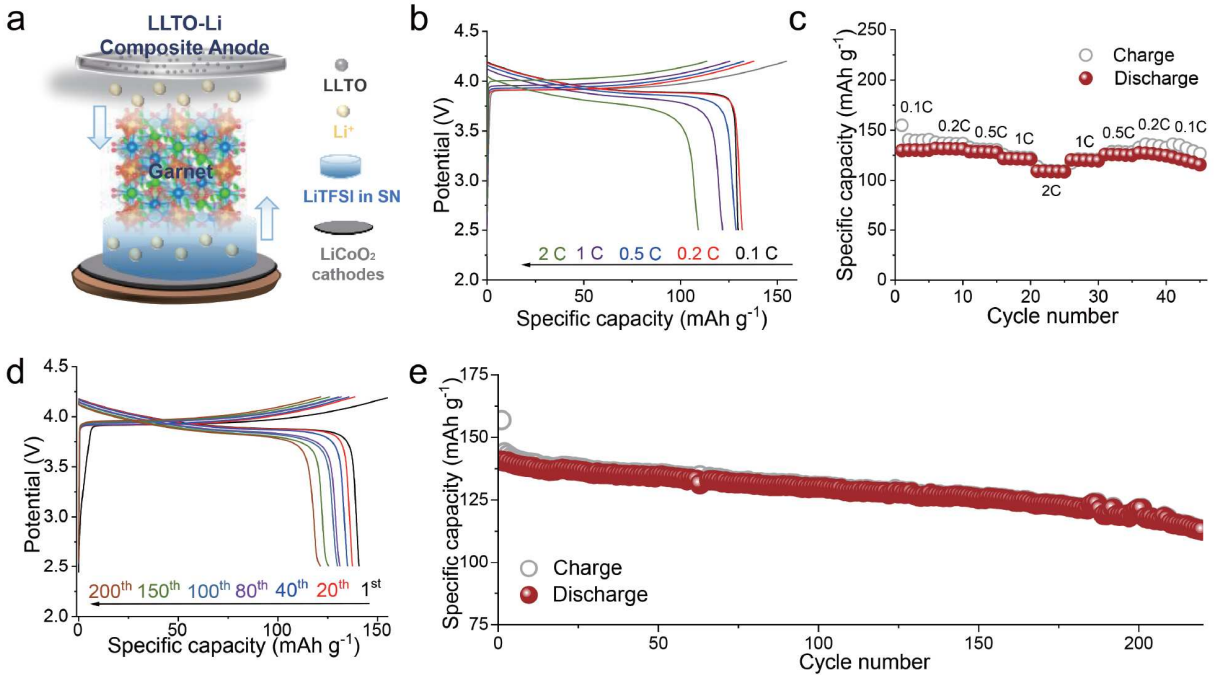

Figure 4 (a) Schematic illustration of the solid-state $LiCoO_2$/AlF_3-LLZTO/Li-LLTO full cell. (b) Galvanostatic charge and discharge curves of the battery at 45 °C. (c) Capacity of the battery under different rates at 45 °C. (d, e) Long-term cycle performance of $LiCoO_2$/AlF_3-LLZTO/Li-LLTO full cells under 0.2 C at 45 °C.

energy storage systems.

Received 16 April 2025; accepted 28 May 2025; published online 9 July 2025

1 Famprikis T, Canepa P, Dawson JA, *et al.* Fundamentals of inorganic solid-state electrolytes for batteries. Nat Mater, 2019, 18: 1278–1291
2 Hu YS. Batteries: getting solid. Nat Energy, 2016, 1: 16042
3 Xiao Y, Wang Y, Bo SH, *et al.* Understanding interface stability in solid-state batteries. Nat Rev Mater, 2019, 5: 105–126
4 Manthiram A, Yu X, Wang S. Lithium battery chemistries enabled by solid-state electrolytes. Nat Rev Mater, 2017, 2: 16103
5 Janek J, Zeier WG. Challenges in speeding up solid-state battery development. Nat Energy, 2023, 8: 230–240
6 Cheng J, Hou G, Sun Q, *et al.* A novel coral-like garnet for high-performance PEO-based all solid-state batteries. Sci China Mater, 2022, 65: 364–372
7 Chang X, Zhao YM, Yuan B, *et al.* Solid-state lithium-ion batteries for grid energy storage: opportunities and challenges. Sci China Chem, 2023, 67: 43–66
8 Murugan R, Thangadurai V, Weppner W. Fast lithium ion conduction in garnet-type $Li_7La_3Zr_2O_{12}$. Angew Chem Int Ed, 2007, 46: 7778–7781
9 Li Y, Han JT, Wang CA, *et al.* Optimizing Li^+ conductivity in a garnet framework. J Mater Chem, 2012, 22: 15357–15361
10 Buannic L, Orayech B, López Del Amo JM, *et al.* Dual substitution strategy to enhance Li^+ ionic conductivity in $Li_7La_3Zr_2O_{12}$ solid electrolyte. Chem Mater, 2017, 29: 1769–1778
11 Han F, Zhu Y, He X, *et al.* Electrochemical stability of $Li_{10}GeP_2S_{12}$ and $Li_7La_3Zr_2O_{12}$ solid electrolytes. Adv Energy Mater, 2016, 6: 1501590
12 Zhao N, Khokhar W, Bi Z, *et al.* Solid garnet batteries. Joule, 2019, 3: 1190–1199
13 Chen S, Hu X, Nie L, *et al.* Recycling of garnet solid electrolytes with lithium-dendrite penetration by thermal healing. Sci China Mater, 2023, 66: 2192–2198
14 Kazyak E, Garcia-Mendez R, LePage WS, *et al.* Li penetration in ceramic solid electrolytes: *operando* microscopy analysis of morphology, propagation, and reversibility. Matter, 2020, 2: 1025–1048
15 Wang MJ, Choudhury R, Sakamoto J. Characterizing the Li-solid-electrolyte interface dynamics as a function of stack pressure and current density. Joule, 2019, 3: 2165–2178
16 Krauskopf T, Dippel R, Hartmann H, *et al.* Lithium-metal growth kinetics on LLZO garnet-type solid electrolytes. Joule, 2019, 3: 2030–2049
17 Han F, Westover AS, Yue J, *et al.* High electronic conductivity as the origin of lithium dendrite formation within solid electrolytes. Nat Energy, 2019, 4: 187–196
18 Han X, Gong Y, Fu K, *et al.* Negating interfacial impedance in garnet-based solid-state Li metal batteries. Nat Mater, 2017, 16: 572–579
19 Krauskopf T, Mogwitz B, Hartmann H, *et al.* The fast charge transfer kinetics of the lithium metal anode on the garnet-type solid electrolyte $Li_{6.25}Al_{0.25}La_3Zr_2O_{12}$. Adv Energy Mater, 2020, 10: 2000945
20 Krauskopf T, Hartmann H, Zeier WG, *et al.* Toward a fundamental understanding of the lithium metal anode in solid-state batteries—an electrochemo-mechanical study on the garnet-type solid electrolyte $Li_{6.25}Al_{0.25}La_3Zr_2O_{12}$. ACS Appl Mater Interfaces, 2019, 11: 14463–14477
21 Krauskopf T, Mogwitz B, Rosenbach C, *et al.* Diffusion limitation of lithium metal and Li–Mg alloy anodes on LLZO type solid electrolytes as a function of temperature and pressure. Adv Energy Mater, 2019, 9: 1902568
22 Yang C, Xie H, Ping W, *et al.* An electron/ion dual-conductive alloy framework for high-rate and high-capacity solid-state lithium-metal batteries. Adv Mater, 2019, 31: e1804815
23 Fu J, Yu P, Zhang N, *et al. In situ* formation of a bifunctional interlayer enabled by a conversion reaction to initiatively prevent lithium dendrites in a garnet solid electrolyte. Energy Environ Sci, 2019, 12: 1404–1412
24 Xu P, Shuang ZY, Zhao CZ, *et al.* A review of solid-state lithium metal batteries through *in-situ* solidification. Sci China Chem, 2023, 67: 67–86
25 Xiong X, Ma X, Lv T, *et al.* Monophase-homointerface electrodes intrinsically stabilize high-voltage all-solid-state batteries. Sci China Chem, 2024, 67: 1729–1739
26 Song Y, Yang L, Zhao W, *et al.* Revealing the short-circuiting mechanism of garnet-based solid-state electrolyte. Adv Energy Mater, 2019, 9: 1900671
27 Shi J, Sun G, Li L, *et al.* Fluorine substitution at the O-site imparts

enhanced chemical stability for garnet-structured electrolytes. ACS Energy Lett, 2022, 8: 48–55
28 Duan J, Wu W, Nolan AM, *et al.* Lithium–graphite paste: an interface compatible anode for solid-state batteries. Adv Mater, 2019, 31: 1807243
29 Du M, Sun Y, Liu B, *et al.* Smart construction of an intimate lithium| garnet interface for all-solid-state batteries by tuning the tension of molten lithium. Adv Funct Mater, 2021, 31: 2101556
30 Wei C, Xiao Y, Wu Z, *et al.* Construction of LiCl/LiF/LiZn hybrid SEI interface achieving high-performance sulfide-based all-solid-state lithium metal batteries. Sci China Chem, 2024, 67: 1990–2001
31 Zhang Y, Yao M, Wang T, *et al.* A 3D hierarchical host with gradient-distributed dielectric properties toward dendrite-free lithium metal anode. Angew Chem Int Ed, 2024, 63: e202403399
32 Wang Q, Zhang Y, Yao M, *et al.* A lithium-selective "OR-gate" enables fast-kinetics and ultra-stable Li-rich cathodes for polymer-based solid-state batteries. Energy Environ Sci, 2025, 18: 2931–2939
33 Xu L, Yao M, Du L, *et al.* Accelerating lithium ion conduction via activated interfacial dipole layer for long-life and high-voltage solid-state lithium-metal battery. J Energy Chem, 2025, 108: 92–100
34 Du L, Zhang Y, Xiao Y, *et al.* A defect-rich carbon induced built-in interfacial electric field accelerating ion-conduction towards superior-stable solid-state batteries. Energy Environ Sci, 2025, 18: 2949–2961
35 He KQ, Liao XG, Lian HJ, *et al.* Endowing rapid Na^+ conduction by architecture design of $Na_3Zr_2Si_2PO_{12}$ in composite electrolytes for ultralong lifespan quasi-solid-state sodium metal batteries. Rare Met, 2025, 44: 3795–3805
36 Zhang Y, Liu H, Liu F, *et al.* Dual-anion-rich polymer electrolytes for high-voltage solid-state lithium metal batteries. ACS Nano, 2025, 19: 3197–3209
37 Alexander GV, Shi C, O'Neill J, *et al.* Extreme lithium-metal cycling enabled by a mixed ion- and electron-conducting garnet three-dimensional architecture. Nat Mater, 2023, 22: 1136–1143
38 Chen CC, Fu L, Maier J. Synergistic, ultrafast mass storage and removal in artificial mixed conductors. Nature, 2016, 536: 159–164
39 Cao C, Zhong Y, Chandula Wasalathilake K, *et al.* A low resistance and stable lithium-garnet electrolyte interface enabled by a multifunctional anode additive for solid-state lithium batteries. J Mater Chem A, 2022, 10: 2519–2527
40 Ko ST, Lee T, Qi J, *et al.* Compositionally complex perovskite oxides: discovering a new class of solid electrolytes with interface-enabled conductivity improvements. Matter, 2023, 6: 2395–2418
41 Sasano S, Ishikawa R, Sánchez-Santolino G, *et al.* Atomistic origin of Li-ion conductivity reduction at $(Li_{3x}La_{2/3-x})TiO_3$ grain boundary. Nano Lett, 2021, 21: 6282–6288
42 Zhang N, Li X, Ye H, *et al.* Oxide defect engineering enables to couple solar energy into oxygen activation. J Am Chem Soc, 2016, 138: 8928–8935
43 Gao X, Fisher CAJ, Kimura T, *et al.* Lithium atom and A-site vacancy distributions in lanthanum lithium titanate. Chem Mater, 2013, 25: 1607–1614
44 Ma C, Chen K, Liang C, *et al.* Atomic-scale origin of the large grain-boundary resistance in perovskite Li-ion-conducting solid electrolytes. Energy Environ Sci, 2014, 7: 1638–1642
45 Deng S, Zhu H, Zheng Z, *et al.* Synergistically engineering grains and grain boundaries toward Li dendrite-free $Li_7La_3Zr_2O_{12}$. Nano Lett, 2024, 24: 9801–9807
46 Wang C, Zeng Z, Qiu P, *et al.* Ultra-wettable liquid metal interface for highly durable solid-state lithium batteries. Matter, 2024, 7: 934–947
47 Zheng H, Li G, Ouyang R, *et al.* Origin of lithiophilicity of lithium garnets: compositing or cleaning? Adv Funct Mater, 2022, 32: 2205778
48 Chen L, Zhang J, Tong RA, *et al.* Excellent Li/garnet interface wettability achieved by porous hard carbon layer for solid state Li metal battery. Small, 2022, 18: e2106142
49 Bi Z, Sun Q, Jia M, *et al.* Molten salt driven conversion reaction enabling lithiophilic and air-stable garnet surface for solid-state lithium batteries. Adv Funct Mater, 2022, 32: 2208751
50 Zhou D, Ren GX, Zhang N, *et al.* Garnet electrolytes with ultralow interfacial resistance by SnS_2 coating for dendrite-free all-solid-state batteries. ACS Appl Energy Mater, 2021, 4: 2873–2880
51 Li X, Ning P, Liu P, *et al.* Enabling fast mass transport in anode by a smartly built-in LiC_6 phase for high-performance solid-state lithium metal batteries. Adv Funct Mater, 2024, 34: 2408447
52 Chen Y, Wang Z, Li X, *et al.* Li metal deposition and stripping in a solid-state battery via Coble creep. Nature, 2020, 578: 251–255
53 Wu JF, Zhou W, Wang Z, *et al.* Building K–C anode with ultrahigh self-diffusion coefficient for solid state potassium metal batteries operating at −20 to 120 °C. Adv Mater, 2023, 35: 2209833
54 Singh DK, Fuchs T, Krempaszky C, *et al.* Overcoming anode instability in solid-state batteries through control of the lithium metal microstructure. Adv Funct Mater, 2022, 33: 2211067
55 Yan H, Tantratian K, Ellwood K, *et al.* How does the creep stress regulate void formation at the lithium-solid electrolyte interface during stripping? Adv Energy Mater, 2022, 12: 2102283
56 Wang J, Zhang S, Song S, *et al.* Enabling a compatible Li/garnet interface via a multifunctional additive of sulfur. J Mater Chem A, 2023, 11: 251–258
57 Guo Z, Li X, Wang Z, *et al.* Revealing the potential of apparent critical current density of Li/garnet interface with capacity perturbation strategy. J Energy Chem, 2023, 79: 56–63
58 Cui J, Kim JH, Yao S, *et al.* Exploration of metal alloys as zero-resistance interfacial modification layers for garnet-type solid electrolytes. Adv Funct Mater, 2023, 33: 2210192
59 Chen L, Tong RA, Zhang J, *et al.* Reactive magnesium nitride additive: a drop-in solution for lithium/garnet wetting in all-solid-state batteries. Angew Chem Int Ed, 2023, 62: e202305099
60 Qiu J, Liu X, Chen R, *et al.* Enabling stable cycling of 4.2 V high-voltage all-solid-state batteries with PEO-based solid electrolyte. Adv Funct Mater, 2020, 30: 1909392
61 Kong ZX, Xiong Z, Wu JF, *et al.* Suppressing ionic-to-electronic conduction transition on cathode interface enables 4.4 V poly(ethylene oxide)-based all-solid-state batteries. ACS Energy Lett, 2025, 10: 287–295

Acknowledgement This work was financially supported by the National Natural Science Foundation of China (22309049), the Natural Science Foundation of Hunan Province (2024JJ4010), and the Science and Technology Innovation Program of Hunan Province (2024RC3107). We thank the Analytical Instrumentation Center of Hunan University for the EELS and XCT measurements.

Author contributions Wu JF and Liu J conceived and directed the research; Zhu H and Deng S conducted the experiments and drafted the manuscript; Kong X and Xiang X helped with the data analysis; Duan Y participated in manuscript revision and provided guidance on figure preparation.

Conflict of interest The authors declare that they have no conflict of interest.

Supplementary information Supplementary materials are available in the online version of the paper.

Jilei Liu received his PhD degree in physics & applied physics (2015) from Nanyang Technological University, Singapore. He is currently a full professor at Hunan University and serves as the associate dean of the College of Materials Science and Engineering. His primary research focuses on the design, optimization and mechanism research of high-performance electrochemical energy storage materials and devices.

Jian-Fang Wu received his PhD degree in materials science from Huazhong University of Science and Technology. He is currently an associate professor at Hunan University. His primary research focuses on solid electrolytes and solid-state batteries.

Huilin Zhu is currently pursuing her Master's degree at Hunan University under the supervision of Professor Jian-Fang Wu. Her research primarily focuses on interfacial conduction of LLZO solid electrolytes.

基于过渡金属离子还原构建内含离子/电子混合导电骨架的Li-LLTO复合负极以实现超快锂扩散

朱惠琳[1], 邓诗维[1], 孔心怡[1], 向兴[2], 段岩[1], 吴剑芳[1*], 刘继磊[1*]

摘要 在锂沉积/剥离过程中，Li/LLZO界面处界面电荷传输稳定性差，且易形成锂枝晶，制约了LLZO固体电解质的应用. 基于$Li_{0.3}La_{0.5}TiO_3$(LLTO)离子导体中Ti^{4+}离子被金属锂原位还原形成电子/离子混合导体，构建了内含三维互联离子/电子混合导电LLTO骨架的自支撑超薄Li-LLTO复合负极. 复合负极对LLZO固体电解质表现出良好的亲和性，实现了11.7 Ω cm^2的低界面阻抗，及高达4.5×10^{-11} cm^2/s的锂自扩散系数，较纯锂提升了约1个数量级；显著增强了Li-LLTO/LLZO界面的稳定性，对称电池临界电流密度提升4倍，稳定循环长达1300 h；实现了高性能固态锂电池，其循环220次后，容量保持率达80%. 该工作不仅提升了锂金属负极在固态电池中应用的性能，更为下一代高能量密度电化学储能系统的设计提供了思路.